9th International Conference on
Photonic Technologies LANE 2016

Laser material processing based on non-conventional beam focusing strategies

Xiaoming Yu[a], Xinya Wang[a], Margaux Chanal[b], Carlos A. Trallero-Herrero[c], David Grojo[b], and Shuting Lei[a,*]

[a]*Department of Industrial and Manufacturing Systems Engineering, Kansas State University, Manhattan, KS 66506, USA*
[b]*Aix-Marseille University, CNRS, LP3 UMR 7341, F-13288 Marseille, France*
[c]*J. R. Macdonald Laboratory, Department of Physics, Kansas State University, Manhattan, KS 66506, USA*

Abstract

Traditional laser-based material processing relies on concentrating laser energy into a single focal spot, and then positioning this spot on the target material. Recent advances in light manipulation and light-matter interaction show the possibility of developing novel processing strategies, such as parallel processing with multiple focal spots, the use of Bessel beams to extend focal range, and direct 3D processing inside semiconductors. In this paper, we report laser micromachining experiments based on these strategies. Applying spatial beam-shaping techniques to generate Bessel beams of various orders and various superpositions, we show that these beams have the advantages of increased processing speed and improved tolerance to surface unevenness compared to focused Gaussian beams. Using a laser with 1.5-µm wavelength and focusing the beam beneath surface, we directly generate 3D structures inside intrinsic silicon wafer, as a first step toward direct 3D manufacturing in semiconductors. The effect of spherical aberration and doping (free carrier density) on the resultant internal damage is also investigated.

© 2016 The Authors. Published by Bayerisches Laserzentrum GmbH

Keywords: Laser meterial processing; Spatial beam shaping; Bessel beams; Femtosecond laser; Nanosecond laser; Silicon

1. Introduction

Laser-based material processing is realized by concentrating laser energy into small spatial dimension in order to achieve above-threshold intensity (fluence) on material surface, usually by the use of convex lenses or microscope objectives. Two issues can be identified in this conventional focusing approach. First, the laser beam formed in the focal region is approximately Gaussian, suffering from short focal range (Rayleigh length) when focal size is down to several micrometers. Consequently, positioning error or variation of material surface height could steer the target region away from laser focus, leading to inconsistency in machining quality. Second, the key benefit of using lasers for material processing is the ability to directly generate three-dimensional (3D) structures inside material. While extensively studied in dielectrics, this 3D machining capability has not been fully established in semiconductors.

In this work, we attempt to address these issues by adopting novel beam focusing strategies, namely spatial beam shaping for the generation of various orders of Bessel beams, and 3D processing of semiconductors with laser wavelengths that are not commonly used for material processing. We first demonstrate the feasibility of using zero-order Bessel beams in femtosecond laser patterning of thin film solar cells. Extension of focal range by orders-of-magnitude is emphasized. Then we use a spatial light modulator (SLM) to generate superpositions of high order Bessel beams. Through micromachining experiments, we show that multiple craters can be generated on material surface, thus multiplying processing speed. Furthermore, the 1+ (-1) superposition can also reduce collateral damage caused by the ring structures in zero-order Bessel beams. Next, we try to address several key issues in 3D processing of silicon, including the compensation of spherical aberration,

* Corresponding author. Tel.: +1-785-532-3731 .
E-mail address: lei@ksu.edu

© 2016 The Authors. Published by Bayerisches Laserzentrum GmbH

characterization methods for observing laser-induced internal damage, and the effect of doping on the morphology of laser modified region.

2. Processing of thin film solar cell with zero-order Bessel beam

We first use a zero-order Bessel beam in femtosecond laser scribing of micro-grooves on CIGS ($CuIn_xGa_xSe_{2y}S_y$) thin film solar cell (Yu et al. 2015). The goal is to selectively remove the molybdenum (Mo) layer on polyimide (PI) substrate. The process is referred to as P1 patterning in industry. Laser patterning with conventional Gaussian focusing suffers from short focal range, characterized by the Rayleigh length, when the focal size is on the single-micrometer level. As will be shown below, simply replacing the Gaussian beam with a Bessel beam can significantly increase depth-of-focus, and therefore improve laser processing system's tolerance to surface height variance and positioning error.

2.1. Experimental setup

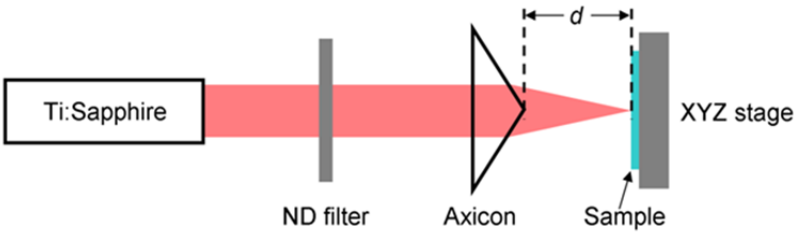

Fig. 1. Experimental setup.

The experimental setup is shown in Fig. 1. A Ti: Sapphire femtosecond laser system delivers pulses with full-width-at-half-maximum (FWHM) pulse duration of 60 fs, center wavelength of 800 nm, maximum pulse energy of 4.3 mJ, beam diameter ($1/e^2$) of 10 mm, and repetition rate of 1 kHz. The pulse energy is attenuated by a variable neutral density (ND) filter. The attenuated beam is focused by an axicon lens (Doric Lenses). This axicon lens is made from fused silica, and has a base angle of 25° and a tip angle of 130°. The thin-film sample used in this study consists of a back contact Mo layer and a PI substrate. The thicknesses of the Mo layer and the PI layer are ~220 nm and 25 µm, respectively. The Mo thin film is deposited on the PI substrate using electron beam evaporation. The sample is mounted on a motorized XYZ stage (Newport). Laser scribing experiments are performed on the sample surface by scanning it across the laser focal spot.

2.2. Bessel beam generated from an axicon lens

Ideally, when an infinite plane wave is used as the input beam, an axicon lens (with an infinite aperture) will generate an ideal Bessel beam, whose transverse intensity distribution, I(r), remains the same at arbitrary axial location, z, i.e., I(r,z) = I(r,0) (Durnin 1987). In our experiment, the input beam has a Gaussian profile, resulting in a Bessel-Gauss beam after the axicon, and its intensity distribution is (Arlt & Dholakia 2000)

$$I(r,z) = I_0 \cdot (4\pi^2 B^2 \frac{z}{\lambda}) \cdot \exp[-\frac{2(Bz)^2}{w_0^2}] \cdot J_0^2(kBr), \tag{1}$$

where I(r,z) is the intensity distribution after the axicon at transverse position (r) and axial position (z), I_0 is the input beam intensity at r=0, λ is the wavelength of the laser, w_0 is the input beam $1/e^2$ radius, J_0 is the zero order Bessel function, k is the wave number (2π/λ), and $B=\sin^{-1}(n\sin A)-A$ is the beam deviation angle, where *n* and A are refractive index (1.45) and base angle (25°) of the axicon, respectively. Some of these variables are illustrated in Fig. 2(a). It should be noted that in the derivation of the above equation, the paraxial assumption, sin (B)~B, is used. For our axicon, B=0.223 rad and sin(B)=0.221, which suggests that the paraxial assumption is valid.

The calculated fluence distribution with 10 µJ pulse energy is shown in Fig. 2(d). Fig. 2(b) shows the fluence along the axial (z) axis at r=0, whereas Fig. 2(c) shows the transverse distribution at z=11 mm, where the on-axis fluence reaches the maximum. From Fig. 2(d) we can see that the central spot size (2.7 µm, measured between the first zeros) remains similar along the z-axis. Fig. 2(e, f) show a comparison between the calculated focus profile and the image of the focal spot seen from a CCD camera at ~3 mm from the tip of the axicon lens. The

measured center spot diameter is about 2.5 μm, which agrees well with the calculated value. The amount of energy contained in the central lobe can be estimated by integrating the intensity distribution (Eq. 2.1 in (Gori et al. 1987)), or by taking the fact that each ring contains approximately the same amount of energy (Turunen & Friberg 2010). Using both methods, we estimate that on a given transverse plane (perpendicular to the z-axis), the central lobe has < 0.1% of the total energy in the input beam (for the configuration shown in Fig. 2(a)). One should note that this small percentage does not mean that energy is wasted. On the contrary, all the input energy contributes to the central lobe, at one z-position or another. In other words, the remaining >99.9% energy is used to form the central lobe at other z locations, and is therefore not wasted.

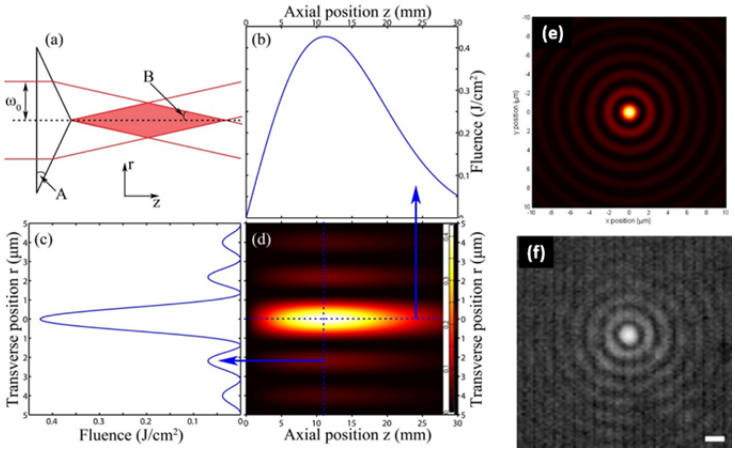

Fig. 2. (a) Schematic of the laser beam focused by an axicon with a base angle (A) of 25°. (b, c) Calculated fluence distribution along the axial and transverse direction, respectively. (d) 2-D plot of fluence distribution. Color bar represents fluence (J/cm^2). Pulse energy is 10 μJ. Please note that in (d) the unit of the axial position z is mm. (e) and (f) are calculated and observed Bessel patterns formed in the focal region, respectively. The scale bar in (f) is 2 μm.

2.3. Experimental results and discussion

With pulse energy of 15 μJ and scanning speed of 0.6 mm/s, lines are written on the sample surface at different positions from the axicon tip (ranging from 1 to 18 mm), as shown in Fig. 3. No damage is observed when the distance is 1 mm. From these images, we can see that when the distance is either small (2-4 mm) or large (16-18 mm), the Mo film is partially removed (indicated by the < 200 nm depth), and the groove shape shows a high variance along the groove direction. In the middle portion of the distance (6-13 mm), the whole Mo layer is removed (indicated by the grooves' depth of 200 nm and their flat bottom). We can see that the groove depth and width remain similar within this distance range from 6 to 13 mm, resulting in a focal range of 7 mm, which is 1000 times longer than convex lenses or microscope objectives for reaching a focus size of 2 μm. The atomic force microscope (AFM) images reveal that within this range, both the groove quality and width are consistent. This demonstrates that axicon lens is a robust choice for consistent scribing quality when fluctuation in sample height or positioning error is significant.

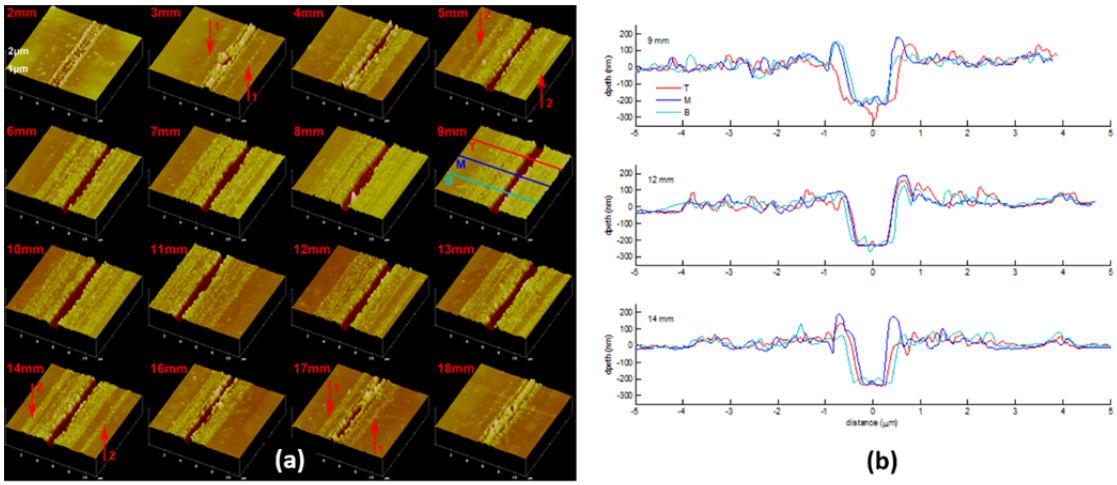

Fig. 3. (a) AFM images of microgrooves fabricated at different distances between the sample surface and the axicon tip at the scanning speed of 0.6 mm/s and pulse energy of 15 μJ. Arrows indicate two pair of lines (numbered 1 and 2) with bump structures, which are undesired collateral damage caused by the ring structures in the beam pattern (see Fig. 6 below and Yu et al. 2015). In the 9 mm figure, T (Top), M (Middle) and B (Bottom) are three positions where cross sections are extracted. Cross sections at similar positions are also extracted in the 12 mm and 14 mm figures. No surface modification is observed for 1 mm, and the image for 15 mm is similar to that for 14 mm. These two images are not shown. (b) Cross sections extracted from (a) along three positions indicated by T (Top), M (Middle) and B (Bottom) at d = 9 mm, 12 mm and 14 mm.

Cross sections are extracted from Fig. 3(a) for the 9 mm, 12 mm and 14 mm grooves, at three positions T (Top), M (Middle) and B (Bottom), and are plotted in Fig. 3(b). At 9 mm, where the ablation effect is found to be maximal, PI substrate is clearly damaged at some location (the red Top curve). Better quality grooves with more uniform widths and reduced substrate damage are observed at 12 mm. At 14 mm, while the substrate damage is small, there is a larger width variation compared to the 12 mm case. More quantitative analysis is needed in the future to characterize the quality of each groove in terms of width, depth, heat affected zone (HAZ), electric insulation, etc.

3. Generating superposed Bessel beam with SLM

In the previous section, a single axicon is used to generate the zero-order Bessel beam. Recent advance in light modulation devices, notably spatial light modulators (SLMs), has made possible the generation of novel beam shapes that are customized and optimized for specific applications. In this section, we apply spatial beam shaping technology to produce superpositions of high-order Bessel beams to improve laser processing speed and reduce collateral damage (Yu et al. 2016).

3.1. Experimental

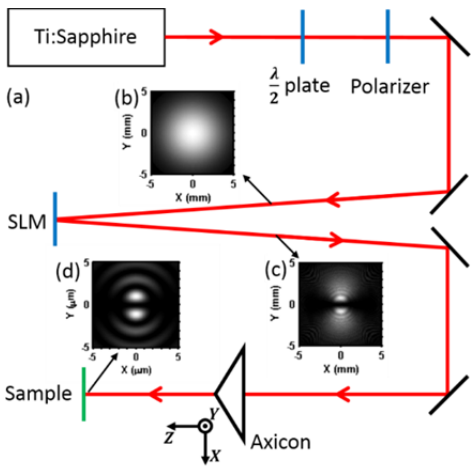

Fig. 4. (a) Experimental setup. Insets are calculated beam shapes (b) in front of SLM, (c) 1.2 m after SLM, and (d) 9 mm after axicon, respectively, for the 1+(1) superposition.

The experimental setup is shown in Fig. 4. We use a Ti: Sapphire femtosecond laser system as our laser source. This system delivers 45 fs (full-width-at-half-maximum, FWHM) laser pulses at a center wavelength of 790 nm and a repetition rate of 2 kHz. At the laser output, the beam has a Gaussian shape with $1/e^2$ diameter of 9.8 mm, and the maximum pulse energy is 2 mJ. A combination of a half-wave plate and a polarizer is used to control pulse energy. The polarizer is oriented along the X-axis, ensuring that the beam is *p*-polarized when shining on the SLM (Hamamatsu X10468-02). The angle between the beam into and out from the SLM is about 1°. The beam coming from the SLM is focused by an axicon (Doric Lenses) with 25° base angle and 25.4-mm diameter. The samples are mounted on a motorized XYZ-stage and move at either high speed (50 mm/s) for single-shot irradiation on borosilicate glass (BK-7) or low speed (1 mm/s) for continuous scribing on molybdenum (Mo) thin film (200-nm thickness). Phase mask images are calculated in Matlab and displayed on the SLM. The generated beam patterns are observed with a CMOS camera (Mightex SME-B050-U) with a constant exposure time (25 ms) and a 30× objective lens mounted in front of the image sensor. During the observation the incoming beam is attenuated by a neutral density filter (ND=4.0) placed after the polarizer. Scanning electron microscope (SEM) and AFM are used to observe the morphology of resultant damage.

3.2. Results and discussion

The center portions of the designed phase masks are shown in Fig. 5(a0)-(a4) and the actually applied masks on the SLM are shown in Fig. 5(b0)-(b4). The pixelation in (b0)-(b4) is due to the finite size of SLM pixels (20 µm × 20 µm). The full size mask is 16 mm × 12 mm. The first mask (a0) is simply a flat phase mask (replicating a flat mirror), and introduces no phase modulation to the input Gaussian beam. The beam after the axicon is a zero-order Bessel-Gaussian beam. The calculated beam pattern is shown in Fig. 5(c0), and the experimentally measured pattern is shown in Fig. 5(d0). This beam generates a single damage spot on borosilicate glass, as shown in Fig. 5(e0).

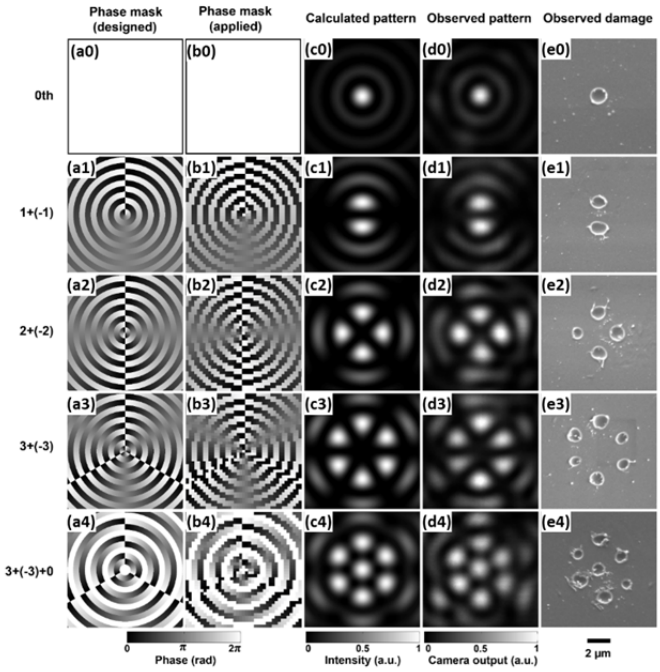

Fig. 5. Center portions of (a0)-(a4) designed and (b0)-(b4) applied SLM phase masks, (c0)-(c4) calculated patterns and (d0)-(d4) observed patterns. The pixelation in (b0)-(b4) is due to the finite size of SLM pixels. All columns represent Bessel beams of increasing superposed orders denoted on the left of the figures. (e0)-(e4) SEM images of damage generated by the corresponding beam patterns on borosilicate glass. The phase mask size shown in (a0)-(a4) and (b0)-(b4) is 800 µm×800 µm, and the width of each ring is 40 µm The full size mask is 16 mm × 12 mm. The size of all the other images is 10 µm×10 µm. All the damage is obtained at about Z=9 mm. Pulse energies (measured in front of SLM) used to generate damage (e0)-(e4) are 100 µJ, 300 µJ, 500 µJ, 600 µJ and 900 µJ, respectively.

The next three masks (a1)-(a3) are used to generate superpositions of Bessel beams with opposite orders of 1 and -1, 2 and -2, and 3 and -3, respectively. The transmission function for these masks, $T_{l,-l}(r,\theta)$, is

$$T_{l,-l}(r,\theta) = exp\left[i(-1)^{\left|\frac{r}{\Delta}\right|} l\theta\right], \tag{2}$$

where l (1, 2 or 3) is the superposed order, r and θ are the radial and azimuthal coordinate, respectively, Δ is the width of each ring, and $\lfloor x \rfloor$ denotes the integer part of the number x. The phase angle of T is calculated at each pixel location, phase-wrapped between 0 and 2 π, and linearly mapped to an 8-bit bitmap image. This image is displayed on the SLM. These masks are composed of concentric rings with continuous azimuthal modulation from 0 (black) to 2π (white). The radial coordinate r is used only to determine the handedness of the azimuthal modulation. Every two neighboring rings have opposite modulation directions (handedness), and the number of modulation cycles (l) along each ring is l=1 for (a-1), l=2 for (a-2) and l=3 for (a3). Similar phase masks have been used to generate high-order Laguerre-Gaussian beams (Matsumoto et al. 2008) and superpositions of Bessel beams when combined with a lens (Vasilyeu et al. 2009). In this study, these rings with opposite modulation are stacked together to ensure that the generated patterns do not rotate as they propagate. These masks generate superpositions of Laguerre-Gaussian beams (e.g., Fig. 4(c)) after the SLM, and these Laguerre-Gaussian beams are focused by the axicon to generate superpositions of Bessel beams with opposite orders, an extension of the work reported previously (Jarutis et al. 2000; Arlt & Dholakia 2000).

Fig. 5(d1)-(d3) show the experimentally observed patterns, which in general match the calculations (Fig. 5(c1)-(c3)). Small differences, such as the elongated shape and unequal brightness of the six spots in (d3), are attributed to slight wavefront distortion originating from the input beam and optical elements. Damage patterns (Fig. 5(e1)-(e3)) are generated with single-pulse exposure.

In Fig. 5(a4), we insert a flat-phase ring between every pair of oppositely-modulated rings. This mask can be seen as a combination of (a0) and (a3), and generates a beam pattern similar to (d3) but with the addition of a central lobe. This new pattern can be considered as a combination of the zero-order Bessel beam and the 3+(-3) superposition. The resultant damage is shown in Fig. 5(e4), where an added damage spot at the center can be seen.

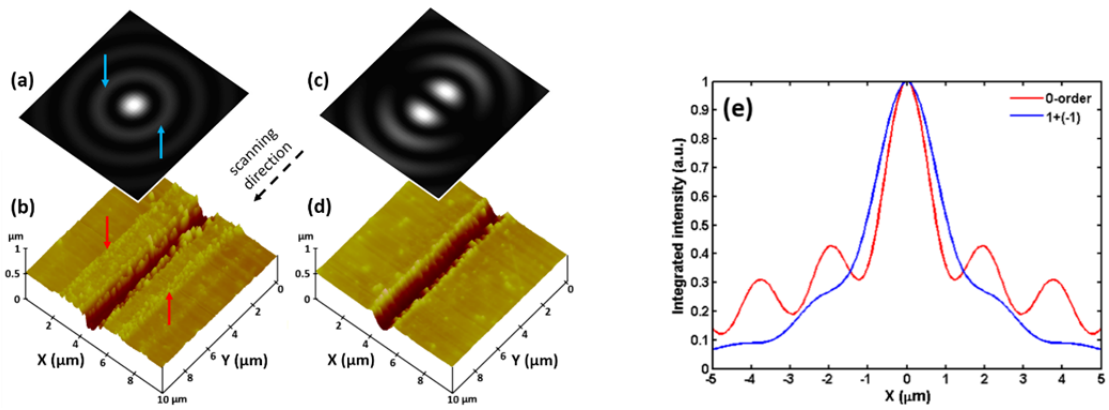

Fig. 6. Comparison of groove scribing with (a, b) zero-order and (c, d) 1+(-1) superposed Bessel beams. (a) and (c) are calculated beam shapes, and (b) and (d) are AFM images of grooves scribed with the corresponding beams. A pair of damage tracks is indicated with red arrows in (b), and is believed to be caused by ring sections indicated by the blue arrows in (a). In both cases, the scanning speed is 1 mm/s, and the samples are placed at Z=9 mm. Pulse energies (estimated peak fluences) are 10 μJ (0.42 J/cm^2) for (b) and 20 μJ (0.38 J/cm^2) for (d). (e) shows a comparison of intensities integrated along the scanning direction between two cases. The integrated intensities are normalized to their peak values.

Besides the ability to simultaneously generate multiple damage spots, the superposed beams can also be used to improve damage morphology. To demonstrate this, we scribe grooves using the zero-order and 1+ (-1) superposed beam, as shown in Fig. 6. We observe a clean groove without any damage tracks for the 1+ (-1) beam. Small bumps observed in Fig. 6(d) are random debris and defects on the surface, not damage from the beam. The improved quality from the superposed beam can also be explained by calculating the intensity profiles integrated along the scanning (Y) direction, as shown in Fig. 6(e). These integrated intensity profiles represent the total power delivered to the sample per unit distance along the X-direction, under the condition that shot-to-shot overlapping is high (> 75% in our case). One can see from Fig. 6(e) that, when the same amount of power is delivered at the center, at locations away from the center ($|X|$ >1 μm), the 1+(-1) beam introduces less power than the zero-order beam. More importantly, the curve for the superposed beam increases monotonically from either side of the X-axis, as opposed to the zero-order beam for which local maxima exist. This is the reason that a distinct groove can be generated with the superposed beam, whereas multiple damage tracks appear for the zero-order beam.

4. 3D processing in silicon

As noted in the Introduction, the ability to directly generate three-dimensional (3D) structures inside materials distinguishes laser-based materials processing from other planar lithographic methods. Current semiconductor manufacturing processes, notably photolithography, are inherently planar methods, and 3D structures are achieved in a layer-by-layer fashion, which involves multiple steps and therefore increases defect rate and reduces yield. Laser-based 3D fabrication provides a one-step manufacturing solution and has the potential to reduce processing time and cost. In this section, we use a commercially available, infrared fiber laser to produce 3D modification in intrinsic and doped silicon wafers, modification that is otherwise inaccessible with commonly used laser wavelengths (e.g., Nd: YAG and Ti: Sapphire) due to linear absorption. Several key issues, such as compensation of spherical aberration and effect of doping concentration, are investigated.

4.1. Experimental

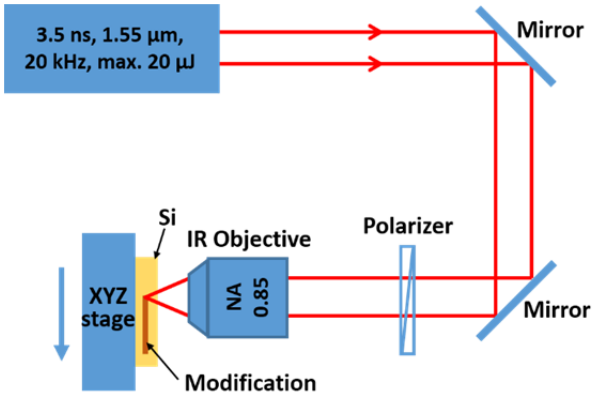

Fig. 7. Experimental setup.

The experimental setup is sketched in Fig. 7. The laser is a fiber MOPA (master oscillator power amplifier) laser (MWTechnologies, Model PFL-1550) delivering laser pulses at 1.55 µm center wavelength and 3.5 ns FWHM (full-width-at-half-maximum of the intensity) pulse duration. The repetition rate is tunable from 20 kHz to 150 kHz, and is fixed at 20 kHz in this study. The maximum pulse energy is 20 µJ. The output beam is collimated and has a $1/e^2$ diameter of 6 mm. It should be noted that the polarization of the output beam is not set by the manufacturer, and our measurements show an elliptical polarization at the output of the laser. A Glan-Taylor polarizer is used in part of the study to allow only linear polarization to pass through. Laser power is adjusted directly on the control unit, and measured before the objective lens. The beam is focused by a 0.85 NA infrared objective lens (Olympus, Model LCPLN100XIR), which has SA correction for silicon thickness of 0-1 mm. The input aperture size of the objective is 3.5 mm, resulting in ~50% energy loss due to beam clipping. The estimated focal spot diameter and confocal length inside silicon are 1.5 µm and 8 µm, respectively. The samples used in this study are (100)-oriented, 1-mm thick silicon wafers, either intrinsic or n/Ph-doped. The intrinsic samples have a resistivity of >200 Ω·cm and are used first in the experiment to find the best focal depth and reveal the damage morphology. Four n-doped samples, with resistivity of 50-100 Ω·cm, 10-14 Ω·cm, 0.5-0.8 Ω·cm and 0.015-0.025 Ω·cm, are used in the latter part of the study to investigate the effect of doping. The wafers are cleaved into small pieces of about 20×20 mm^2 and mounted on a motorized XYZ stage (Newport, Model ILS100PP). The focal depth is controlled by moving the sample along the laser beam's axial direction, and modification is induced by scanning the sample transversely at a constant speed of 1 mm/s. The focus overlapping is > 97% at this speed. The sample after laser writing is cleaved perpendicularly to the scanning direction and the cross sections (in the (110)-plane) are observed with a visible-light microscope. The cleaved surface is then gently polished and examined with the microscope again (no modification is observed). The polished surface is etched in a 50% wt KOH solution for 5 minutes (in an ultrasonic bath) to reveal the modified regions and observed with the microscope. In this study, damage is not observed on either front or back surface of the silicon samples.

4.2. Optimal focal depth with spherical aberration (SA) correction

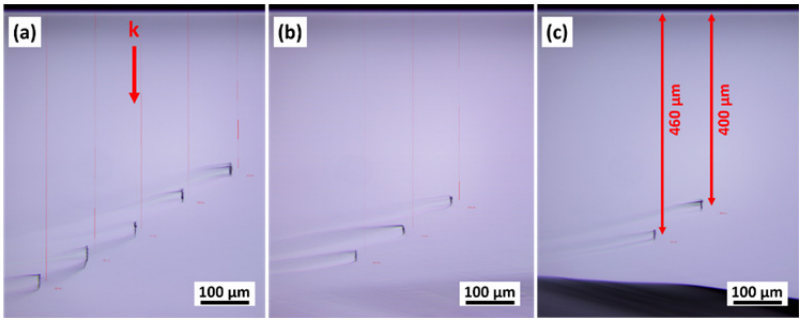

Fig. 8. Cross sections of modification lines in silicon at various depths with pulse energy (measured before the objective lens) of (a) 2.5 µJ, (b) 2 µJ, and (c) 1.5 µJ. Regions in black color and aligned vertically are laser-induced modification. Narrow vertical lines in red color are depth measurements.

Due to the large difference of refractive indices between air and silicon, spherical aberration is expected to be significant and needs to be compensated. The objective lens used in this study has a correction collar and can compensate aberration in silicon with thickness up to 1 mm, which is also the thickness of our samples. To facilitate later characterization of induced modification, we choose to generate modification in the middle of the samples, and therefore the correction collar is set at 0.5 mm throughout the experiments. It should be noted that setting the correction at 0.5 mm does not guarantee optimal focusing at this depth (shown below), since the lens might be designed for wavelengths different from our laser wavelength. To get this optimal focusing depth, we write continuous lines at various depths with 50 µm increments, at a constant speed of 1 mm/s. The samples are then cleaved perpendicularly to the writing direction, and the cross sections are examined with a visible-light microscope. The results for three pulse energies are shown in Fig. 8. Pulse energies in Fig. 8 and in all the following figures are measured before the objective lens, without taking into account energy loss at the objective aperture and air-Si interface. The polarizer is not used in obtaining Fig. 8. Regions in black color and aligned vertically are laser-induced modification, and the structures seen outside these regions are caused by the cleaving procedure. For a high pulse energy of 2.5 µJ, modification is observed within a wider depth range, from 350 to 550 µm. This range reduces for a lower energy of 1.5 µJ, and only two modification spots at 400 and 460 µm can be observed. No modification is seen when the pulse energy is reduced to 1 µJ. These results indicate that the optimal focusing is reached at a depth around 430 µm. Simulation results (not shown here) confirm this conclusion.

4.3. Morphology of resultant modification

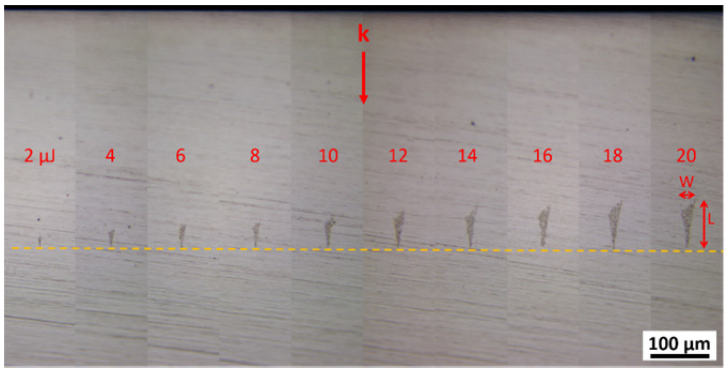

Fig. 9. Laser-induced modification at the same depth (400 µm) and with increasing pulse energy. The horizontal dashed line marks the focusing depth. Laser polarization is random. Width (W) and length (L) of modified region are measured as depicted. Numbers above modified regions represent pulse energy in µJ.

Absorption of 1.55 µm wavelength light in silicon has been attributed to two-photon absorption (Verburg et al. 2014), different from the 6-photon process for 800 nm wavelength and fused silica. Therefore, the volume of absorbed energy is expected to be less confined than the latter case. The nature of absorption is further complicated by the small difference between the photon energy (0.8 eV) and the bandgap (1.1 eV), as it has been noted that the heating of silicon by the laser may cause the bandgap to shrink, leading to linear absorption (Verburg et al. 2014). It is therefore necessary to quantify the size and volume of absorption regions.

To this end, we focus the beam at a fixed depth of 400 µm and write lines with increasing pulse energy. The cross sections treated after the polishing-etching procedure are shown in Fig. 9. The horizontal dashed line marks the intended focal depth of 400 µm. Although it is difficult to determine its exact depth, the focus should reside within or in the vicinity of the modification induced by the lowest pulse energy (2 µJ). The same focal depth is maintained throughout this sample with an accuracy better than 20 µm. Larger modified regions are seen with increasing pulse energy, as would be expected. However, these regions enlarge asymmetrically, towards only the laser beam incoming direction. The modification from high pulse energies shows an inverted-triangle shape. These results suggest that the energy is absorbed in the region before the geometric focus (on the plane marked by the dashed line). Since the maximum peak power delivered inside silicon is 2 kW, an order of magnitude below the critical power for self-focusing, collapse of the laser beam is not responsible for the increase of modification size. A simple estimate of the total energy confined in the modified volume shows that the highest energy density can reach 4.6 kJ/cm^3 (with the consideration of energy loss at objective lens and air-Si interface), high enough for silicon to reach the melting temperature (1687 K). However, the increased modification size with increasing pulse energy is undesired for localization of laser energy and high-precision laser processing. It is crucial to understand the fundamental mechanisms in the laser energy deposition process in order to realize 3D fabrication capabilities in semiconductors.

4.4. Effect of doping

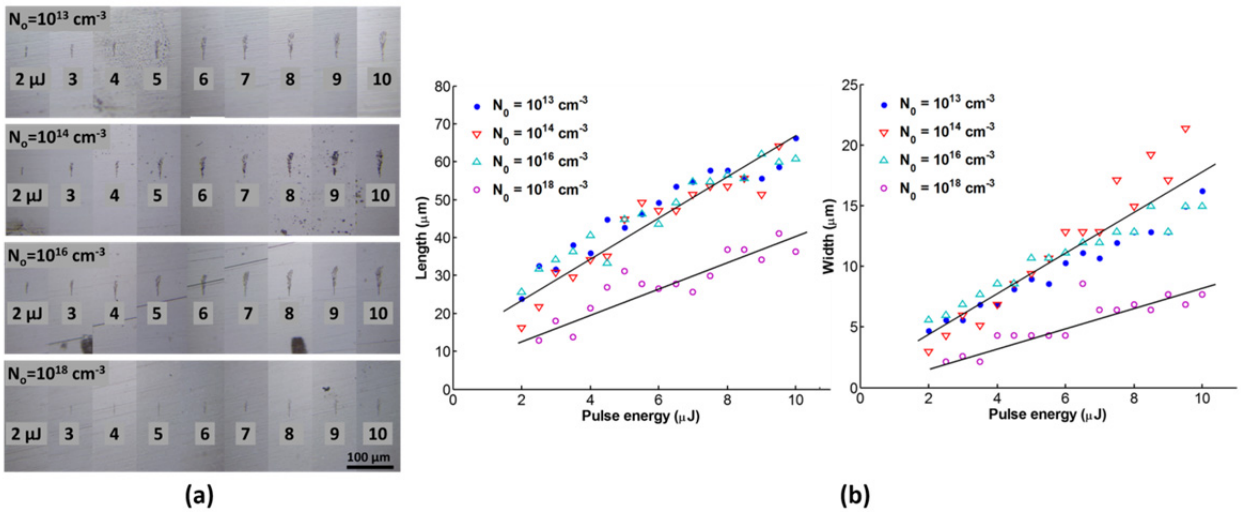

Fig. 10. (a) Laser-induced modification in silicon wafers with various level of doping (free carrier density, N_o, indicated in the top left of each subfigure). Pulse energy is indicated on the bottom of each modification. (b) Measured length and width of modified region at various doping levels. Solid lines are a guide to the eye.

In Leyder et al. (2013) it has been shown that localized nonlinear absorption can be achieved in doped silicon with free carrier density up to 10^{18} cm^{-3}. However, due to the increased linear absorption at high doping levels, laser energy reached at the focus is expected to decrease since light is absorbed before it reaches the focus. In this section, we investigate the effect of doping (free carrier density, N_0) on the resultant modification. Four samples with free carrier concentration of 10^{13}, 10^{14}, 10^{16} and 10^{18} cm^{-3} are used. During the laser treatment, the focal depth is maintained at about 460 µm with an accuracy better than 20 µm among these samples, ensuring that the focus distortion due to spherical aberration is small. Other experimental conditions, such as scanning speed and the amount of time for chemical etching, are kept the same. Optical images of etched cross sections in doped silicon are shown in Fig. 10(a), and measured lengths and widths are shown in Fig. 10(b). Both of the figures show results as a function of doping and energy per pulse. Note that in obtaining Fig. 10 the polarizer is inserted to allow linear polarization (perpendicular to the scanning direction) to pass through. Results from the orthogonal linear polarization (parallel to the scanning direction) are similar and are not shown here.

From Fig. 10(a) we can see that, at each pulse energy, the shape of modified region are similar for N_0=10^{13}, 10^{14} and 10^{16} cm^{-3}. Small differences in the shape and the contrast between the modified and surrounding regions are attributed to variations in the polishing and etching process. This observation is confirmed in Fig. 10(b), where the measured lengths and widths show a similar, linear relationship with pulse energy. The similarity of resultant modification at lower dopant concentrations suggests an energy absorption mechanism independent of initial free carrier densities, in consistency with a previous study (Leyder et al. 2013). As N_0 increases to 10^{18} cm^{-3}, we observe significant reduction in both modification size and contrast. While the lengths and widths also

show a nearly linear relationship, the values are halved at each pulse energy compared to the other three samples. No modification is seen at 2 μJ pulse energy. This behavior can be understood if we take into account the appearance of linear absorption at high carrier densities of 10^{18} cm^{-3}. As has been shown previously (Leyder et al. 2013), linear absorption becomes significant at this concentration. In fact, we find that the 50% reduction in length and width agrees quantitatively well with the amount of linear absorption (~40%) though a thickness of 500 μm (similar to the focal depth used in this study), assuming that modification length and width increase linearly with pulse energy.

5. Conclusion and outlook

We demonstrate here the feasibility and advantages of applying novel beam focusing strategies in laser material processing. By replacing the commonly used Gaussian beam with various types of Bessel beams, we greatly extend focal range and improve the robustness of laser processing system. The 3D machining capability in intrinsic and doped silicon is also explored, which could potentially transform current semiconductor fabrication technologies. Based on a fundamental understanding of light-matter interaction, and equipped with the above-mentioned and other techniques to control laser material processing (Yu, Bian, Zhao, et al. 2013; Yu, Bian, Chang, et al. 2013; Yu et al. 2014), we foresee a future when lasers could be customized in multiple dimensions (spatial, temporal and spectral) for specific applications (cutting, drilling, surface texturing, etc.), and eventually become a manufacturing tool that is used as naturally and efficiently as mechanical tools are used nowadays, but for more challenging tasks.

Acknowledgements

Financial support of this work by the National Science Foundation under Grant No. CMMI-1131627 is gratefully acknowledged. C. T-H and laser support is provided by the Chemical Sciences, Geosciences, and Biosciences Division, Office of Basic Energy Sciences, Office of Science, U.S. Department of Energy (DOE) under Grant No. DE-FG02-86ER13491.

References

Arlt, J. & Dholakia, K., 2000. Generation of high-order Bessel beams by use of an axicon. Optics Communications, 177(1-6), pp.297–301.

Durnin, J., 1987. Exact solutions for nondiffracting beams. I. The scalar theory. JOSA A, 4(4), pp.651–654.

Gori, F., Guattari, G. & Padovani, C., 1987. Bessel-Gauss beams. Optics Communications, 64(6), pp.491–495.

Jarutis, V., Paškauskas, R. & Stabinis, A., 2000. Focusing of Laguerre–Gaussian beams by axicon. Optics Communications, 184(1-4), pp.105–112.

Leyder, S. et al., 2013. Non-linear absorption of focused femtosecond laser pulses at 1.3μm inside silicon: Independence on doping concentration. Applied Surface Science, 278, pp.13–18.

Matsumoto, N. et al., 2008. Generation of high-quality higher-order Laguerre-Gaussian beams using liquid-crystal-on-silicon spatial light modulators. Journal of the Optical Society of America. A, 25(7), pp.1642–51.

Turunen, J. & Friberg, A.T., 2010. Chapter 1 – Propagation-Invariant Optical Fields. In Progress in Optics. pp. 1–88.

Vasilyeu, R. et al., 2009. Generating superpositions of higher-order Bessel beams. Optics express, 17(26), pp.23389–95.

Verburg, P.C., Römer, G.R.B.E. & Huis in 't Veld, A.J., 2014. Two-photon–induced internal modification of silicon by erbium-doped fiber laser. Optics Express, 22(18), pp.21958–21971.

Yu, X. et al., 2014. Fabricating nanostructures on fused silica using femtosecond infrared pulses combined with sub-nanojoule ultraviolet pulses. Optics letters, 39(19), pp.5638–40.

Yu, X., Bian, Q., Chang, Z., et al., 2013. Femtosecond laser nanomachining initiated by ultraviolet multiphoton ionization. Optics express, 21(20), pp.24185–90.

Yu, X., Bian, Q., Zhao, B., et al., 2013. Near-infrared femtosecond laser machining initiated by ultraviolet multiphoton ionization. Applied Physics Letters, 102(10), p.101111.

Yu, X., Ma, J. & Lei, S., 2015. Femtosecond laser scribing of Mo thin film on flexible substrate using axicon focused beam. Journal of Manufacturing Processes.

Yu, X., Trallero-Herrero, C.A. & Lei, S., 2016. Materials processing with superposed Bessel beams. Applied Surface Science, 360, p.833.